

# A boundary integral equations approach to electrical impedance tomography: experiments on the KTC2023 data

Spyros Alexakis<sup>1</sup>, Adam Stinchcombe<sup>1</sup>, and Teemu Tyni<sup>2</sup>

<sup>1</sup>Department of Mathematics, University of Toronto, Canada

<sup>2</sup>Research Unit of Applied and Computational Mathematics,  
University of Oulu, Finland

## Abstract

In the fall of 2023 the Finnish Inverse Problems Society organized the Kuopio Tomography Challenge 2023 (KTC2023, see <https://www.fips.fi/KTC2023.php>). The aim of KTC2023 was to gather groups of contestants and test their various reconstruction methods on real electrical impedance tomography data. The main purpose of this paper is to demonstrate a boundary integral equation method (BIEM) based forward solver on the KTC2023 challenge data set. We also briefly summarize our BIEM formulation of the complete electrode model of electrical impedance tomography, as presented in the authors' previous work, and discuss its numerical implementation.

## 1 Introduction

In December 2023 the Finnish Inverse Problems Society (FIPS) organized the Kuopio Tomography Challenge 2023 (KTC2023, see <https://www.fips.fi/KTC2023.php>), in which the aim was to gather groups of contestants and test various reconstruction methods on real electrical impedance tomography (EIT) data. The purpose of this paper is to demonstrate a boundary integral equation method based forward solver recently developed by the authors in [25] on this challenge data set.

Electrical impedance tomography is characterized as the problem of recovering the electric conductivity distribution inside an unknown body from electric current and voltage measurements performed at the boundary of the target. Mathematically, the question is about recovering the conductivity coefficient  $\sigma(x) > 0$  in the partial differential equation

$$\nabla \cdot (\sigma(x)\nabla u) = 0, \quad x \in \Omega_0, \quad (1)$$

in which  $u$  is the electrostatic potential, given suitable boundary measurements of  $u$ . Let us introduce the notation we use for EIT next. The most realistic model of EIT is the so-called complete electrode model (CEM), where the boundary conditions for (1) are given by

$$\begin{cases} \partial_n u = 0, & x \in \partial\Omega_0 \setminus \cup_{k=1}^L e_k, \\ u(x) + \sigma z_k \partial_n u(x) = U_k, & x \in e_k, \\ \int_{e_k} \sigma \partial_n u \, dl_x = I_k, \end{cases} \quad (2)$$

in which the electrodes are modelled by open and connected sets  $e_k \subset \partial\Omega_0$  with  $e_i \cap e_j = \emptyset$ ,  $i \neq j$ ;  $z_k > 0$  are the contact impedances of the electrodes; and  $I_k$  are the total currents injected through each electrode, for  $n = 1, \dots, L$ . The constants  $U_k \in \mathbb{R}$ ,  $k = 1, \dots, L$  are the unknown voltages arising from the (known) current injections  $I_k$ . For existence of a solution  $u \in H^1(\Omega_0)$  it is required that the total injected current  $\sum_{k=1}^L I_k = 0$ , while the condition  $\sum_{k=1}^L U_k = 0$  fixes a unique solution. The measurement data in the inverse problem of recovering  $\sigma$  is the current-to-voltage map

$$R : (I_1, \dots, I_L) \mapsto (U_1, \dots, U_L).$$

In real world applications, the electrodes only cover parts of the outer boundary  $\partial\Omega_0$  and the task of recovering  $\sigma$  is highly ill-posed, see [18, 26].

Many uses of EIT, and the challenges therein, are highlighted in the survey [26]. We mention here some uses in medical imaging, such as, stroke detection [2] and brain imaging [3, 7], lung and heart monitoring [15, 16], and breast cancer detection [4]. Recently, steps have also been taken towards recovering possibly unknown boundary shapes simultaneously along with the contact impedances and conductivity distribution [1].

In KTC2023, several target bodies (both conductive and resistive) were placed inside a water tank and the EIT problem is that of locating these inclusions given only (limited) current-to-voltage measurements. The quantitative evaluation of the contestant's methods was performed by a comparison against a ground truth (segmentation of a photograph of the water chamber) using a structural similarity index measure (SSIM). For details of the evaluation method we refer to [20]. The results of the challenge were published in December of 2023. Two winners of KTC2023 were machine learning based: 1st place (University of Bremen, Germany and University College London, The United Kingdom) used post-processing UNet for EIT segmentation, and the 2nd place (The Federal University of ABC, Brazil) a post-processing smoothness prior EIT reconstructions using convolutional neural networks. The 3rd place (The Technical University of Denmark, Denmark) took a more direct approach via a level set method based on [8].

Our present strategy is based on a boundary integral equation method. Such methods are not new to EIT and, for example, point-electrode models have been proposed in [12, 11] and integral equations for the complete electrode model in [13]. Our aim in this paper is to present a novel BIEM based forward solver, and

use it to show that boundary integral equations can be a useful tool particularly for detecting inclusions. Moreover, boundary integral equation based forward solvers are fast compared to finite element methods (for some comparisons, see [25]), because they do not require fine triangulations of possibly complicated domains. Therefore, they have potential uses for example in iterative solvers for EIT, and for forward solvers in network training.

This paper is organized as follows. In Section 1.1 we derive the boundary integral equation formulation for the complete electrode model using single layer potentials. Section 2 discusses briefly the numerical and computational aspects of the integral equations. Finally, in Section 3 we cover the inverse problem and perform experiments on the KTC2023 dataset.

## 1.1 Derivation of the boundary integral equations

In this work we use the recently developed (see [25]) boundary integral equation method (BIEM) for solving the equations (1)-(2). Let  $\Omega_0 \subset \mathbb{R}^2$  be a compact domain with a smooth boundary and let  $\Omega_i \subset \Omega_0$ ,  $i = 1, 2, \dots, N$  be domains with smooth boundaries. We will assume that the conductivity  $\sigma(x)$  is constant  $\sigma_i$  within each domain  $\Omega_i$  and equal to  $\sigma_0$  in  $\Omega_0 \setminus (\bigcup_{i=1}^N \Omega_i)$ . To complete the equations (1)-(2) in case of piecewise constant conductivity, we require that the matching conditions

$$\begin{aligned} [u] &= 0, & x \in \partial\Omega_i, & i = 1, \dots, N, \\ [\sigma \partial_n u] &= 0, & x \in \partial\Omega_i, & i = 1, \dots, N \end{aligned} \quad (3)$$

hold on the interfaces  $\partial\Omega_i$ . Here we used the notation  $[\xi](x) = \xi^+(x) - \xi^-(x)$ , where  $\xi^+(x_0)$  (resp.  $\xi^-(x_0)$ ) is the limit of  $\xi(x)$  as  $x \rightarrow x_0$  from  $\Omega_0 \setminus \Omega_i$  (resp. from  $\Omega_i$ ). In case two or more domains  $\Omega_i$  overlap, we define the conductivity in the overlap region to be the sum of overlapping conductivities:

$$\sigma(x) := \begin{cases} \sum_{i=1}^N \sigma_i \chi_i(x), & x \in \bigcup_{i=1}^N \Omega_i \\ \sigma_0, & x \in \Omega_0 \setminus \bigcup_{i=1}^N \Omega_i, \end{cases}$$

in which  $\chi_i(x) = 1$  if  $x \in \Omega_i$  and  $\chi_i(x) = 0$  otherwise is an indicator function for the body  $i$ . The equation (1) with the conditions (2)-(3) is then well-posed in  $H^1(\Omega_0)$  (see e.g., [19, 22]).

We next re-express the electrostatic potential  $u$  of the CEM (1)-(3) in terms of single layer potentials as

$$u(x) = \sum_{j=0}^N S_{\partial\Omega_j}[\gamma_j](x), \quad (4)$$

in which  $\gamma_j$  is the charge density of the interface  $\partial\Omega_j$  and the single layer potential  $S_{\partial\Omega_j}[\gamma_j]$  is given by

$$S_{\partial\Omega_j}[\gamma_j](x) := \int_{\partial\Omega_j} G(x, y) \gamma_j(y) \, dl_y.$$

The kernel

$$G(x, y) := \frac{1}{2\pi} \log(|x - y|)$$

is harmonic and weakly singular. The charge density and the potential  $u$  are connected by

$$\gamma_i = [\partial_n u] = \partial_{n^+} u - \partial_{n^-} u, \quad \text{on } \partial\Omega_i, \quad i = 1, \dots, N.$$

It is well-known (see [9, 17]) that the normal derivative of the single layer potential satisfies

$$\partial_{n^\pm} S_{\partial\Omega_i}[\gamma_i](x) = K_{\partial\Omega_i}^*[\gamma_i](x) \pm \frac{1}{2}\gamma_i(x), \quad x \in \partial\Omega_i,$$

with

$$K_{\partial\Omega_i}^*[\gamma_i](x) := \frac{1}{2\pi} \int_{\partial\Omega_i} \frac{(x - y) \cdot n(x)}{|x - y|^2} \gamma_i(y) \, dl_y, \quad x \in \partial\Omega_i$$

is the adjoint Neumann-Poincaré operator. This allows us to write

$$\partial_{n^\pm} S_{\partial\Omega_j}[\gamma_j](x) = \int_{\partial\Omega_j} K(x, y) \gamma_j(y) \, dl_y \pm \frac{1}{2}\gamma_j(x) \delta_{ij}, \quad x \in \partial\Omega_i, \quad i = 0, \dots, N,$$

in which  $\delta_{ij}$  is the Kronecker delta symbol and where we denote

$$K(x, y) := \frac{(x - y) \cdot n(x)}{2\pi|x - y|^2}.$$

We observe that  $K(x, y)$  has a removable singularity on the diagonal, provided  $\partial\Omega_i$  is  $C^2$ -smooth. The singularity is removed by defining  $K(x, x) = \frac{\kappa(x)}{4\pi}$ , where  $\kappa(x)$  is the curvature at point  $x \in \partial\Omega_i$ , and with this  $K$  becomes a continuous function.

Under these notations the complete electrode model (1)–(3) can be expressed as integral equations for the charge densities  $\gamma_i$  as follows.

**Off electrodes:**

$$-\frac{1}{2}\sigma(x)\gamma_0(x) + \sigma(x) \sum_{j=0}^N \int_{\partial\Omega_j} (K(x, y) - \delta_{0j}) \gamma_j(y) \, dl_y = 0, \quad x \in \partial\Omega_0 \setminus \bigcup_{k=1}^L e_k. \quad (5)$$

**On electrodes:**

$$-\frac{1}{2}z_k\sigma(x)\gamma_0(x) + \sum_{j=0}^N \int_{\partial\Omega_j} (G(x, y) + z_k\sigma(x)K(x, y)) \gamma_j(y) \, dl_y = U_k, \quad (6)$$

for  $x \in e_k$ ,  $k = 1, \dots, L$ ;

$$\int_{e_k} \left( -\frac{1}{2}\sigma(x)\gamma_0(x) + \sigma(x) \sum_{j=0}^N \int_{\partial\Omega_j} K(x, y) \gamma_j(y) \, dl_y \right) dl_x = I_k,$$

for  $k = 1, \dots, L$ .

**On interfaces:**

$$\frac{1}{2}(\sigma^+(x) + \sigma^-(x))\gamma_i(x) + (\sigma^+(x) - \sigma^-(x)) \sum_{j=0}^N \int_{\partial\Omega_j} K(x, y)\gamma_j(y) \, dl_y = 0, \quad (7)$$

for  $x \in \partial\Omega_i$ ,  $i = 1, \dots, N$ . Here the symbols  $\sigma^\pm(x)$  denote the conductivity in the direction  $\pm n(x)$ . In (5) the kernel  $K(x, y)$  has been replaced by  $K(x, y) - \delta_{0j}$  as in [5, 25]. This choice (5) with  $\sum_{k=1}^L I_k = 0$  results in a unique solution to the system of integral equations, and also forces

$$\int_{\partial\Omega_0} \gamma_0(x) \, dl_x = 0.$$

Finally, the same integral equations hold in case the interfaces are only assumed to be Lipschitz. In this work we consider interfaces that are either smooth or piecewise  $C^2$ , for instance, polygons. In case some domains  $\Omega_i$  overlap, we require that the intersection of the interfaces  $\partial\Omega_i$  is transverse to avoid cusps, where the behaviour of the integral equations and the electrostatic potential is unknown.

## 2 Numerical implementation

The numerical implementation of the BIEM we use was developed in [25] and we recall here the main points. To discretize the integral equations (5) – (7) we used the Nyström method. The interfaces  $\partial\Omega_i$  are first parametrized by  $q \in [0, 1)$  and then discretized by taking a grid of  $M_i > 0$  points  $q_j^i$ ,  $j = 0, \dots, M_i - 1$ . Two different discretization schemes are used depending on the type of interface. We call a curve parametrized over  $[0, 1)$  *panelled*, when the curve is split into subsegments, called panels, parametrized over  $[x_i, x_{i+1})$  for  $0 = x_1 < \dots < x_K = 1$  for some  $K \in \mathbb{N}$ . The points on the curve evaluated at  $x_1, \dots, x_K$  are called panel breaks. Numerical integration over a panelled curve can then be performed over each panel separately using suitable quadrature rules.

In our implementation, the outer interface and any interfaces overlapping each other are broken into panels. We ensure that panel breaks are located at the electrode boundaries on the outer interface, and at any intersection points (found automatically by using a quasi-Newton algorithm) of two interfaces. The panels neighboring these intersection points or electrode boundaries are further subdivided dyadically as follows: a panel over  $[a, b)$  is divided into two new panels over  $[a, (b+a)/2)$  and  $[(b+a)/2, b)$ , and this subdivision is repeated recursively on the panels adjacent to any intersection points or corners, see [14]. Moreover, interfaces within a specified threshold distance from each other are also panelled. Panelled interfaces are equipped with Gauss-Legendre quadrature nodes on each panel, while on non-panelled interfaces we use the uniformly distributed quadrature nodes given by trapezoidal rule, yielding exponential convergence when the interface is distant enough from other interfaces [24].

We give emphasis on the fact that the kernel  $G(x, y) + z_k \sigma(x) K(x, y)$  in (6) has a logarithmic singularity, requiring a more specialized choice of quadrature for its accurate numerical evaluation. The arising singular integrals are evaluated by introducing an auxiliary set of nodes  $\{x_i\}$  and weights  $\{w_i\}$  according to a generalized Gaussian quadrature [6]. The determination of the quadrature nodes and weights requires solution of a nonlinear optimization problem, and the calculation is carried out using GGQ available at <https://github.com/JamesCBremerJr/GGQ>. To obtain the values of the integrands involved in the singular integrals at the auxiliary nodes we use Lagrange interpolation from the Gauss-Legendre or uniform nodes, see [23]. We mention also [10] for quadrature methods for these types of weakly singular integrals.

Finally, the discretized integral equations (5) – (7) can be written as the single linear system

$$\mathbf{A}\mathbf{g} = \mathbf{I}, \quad \mathbf{g} \in \mathbb{R}^{M+L}, \quad (8)$$

where  $M = \sum_{i=0}^N M_i$  is the total number of grid nodes and the right-hand side  $\mathbf{I} = (0, \dots, 0, I_1, \dots, I_L)^T \in \mathbb{R}^{M+L}$  contains the injected currents. These equations are solved via Gaussian elimination with partial pivoting, allowing the right-hand side  $\mathbf{I}$  be a matrix  $\bar{\mathbf{I}} := (\mathbf{I}_1, \dots, \mathbf{I}_m)$  corresponding to several injected current patterns, simultaneously. The solution  $\mathbf{g}$  contains both values of the charge densities  $\gamma_j$  at the nodes  $q_i$ , and the values of the electrode potentials  $U_k$  directly, providing ready access to the voltage measurements without a need to evaluate the electrostatic potential  $u$  through the single layer potential expression (4).

Finally, for flexibility, we have implemented all of our quadratures in an adaptive way. More precisely, we used either a Fourier or Legendre series based methods to study the accuracy of the solution to (8). On interfaces with uniform grids we expanded the found  $\gamma$  into Fourier series via the fast Fourier transform. If the highest Fourier coefficients are below a specified threshold, we accept the solution, if not we refine those interfaces. Similar study is done on panels with Gaussian quadrature nodes, but instead of Fourier coefficients we studied the size of the Legendre series coefficients of  $\gamma$ . In case the number of quadrature nodes on a panel (or interface) exceeds a specified threshold, we further subdivide the panel (or interface) dyadically. More details on the adaptive methods can be found in [5, 25].

## 3 Inverse problem of EIT

### 3.1 Description of the measurement setup

The measurement data is described in detail in [20], but we briefly recall the setup here for the reader’s convenience. The target is a cylindrical plastic water tank with inner diameter of 23.0 cm, with 32 stainless steel electrodes of height<sup>1</sup> 5.0 cm placed at the boundary of the water tank, and with various inclusions

<sup>1</sup>This information was obtained in private communication with the organizers of KTC2023.

placed within the tank. Each of the electrodes (and the gaps between electrodes) covered an angle of 5.625 degrees, and depth of water was 5.0 cm. The units of the raw measurement data were mA (milliamperes) and V (volts). The inclusions placed in the tank were either conductive (conductive 3D printed plastic or metal) or resistive (3D printed PLA plastic) compared to the background water. The measurement data was the voltage differences between specified electrodes. The data can be found in [21].

The challenge data is organized in the following way. Four practise targets were provided with full 32 electrode data (we call these targets Level 0). In the challenge, the algorithms were tested on new data not available to participants. The data was organized by difficulty levels such that at Level 1 the full 32 electrode data was provided and at each increase of difficulty level the number of active measurement electrodes was reduced by 2 (e.g., at Level 7 twelve electrodes were not used in the measurements). At each challenge level there were three configurations of inclusions, labelled A, B, and C. At all challenge levels, a set of reference voltages arising from measurement using all electrodes in a chamber containing only water was provided.

### 3.2 Iterative least squares solver for EIT

To experiment on the experimental data provided in KTC2023, we employ a straightforward least-squares approach. We are given the experimental voltages  $V_{\text{exp}}$  arising from the current injections. To combat against possible systematic errors in the measurement data, we use the provided reference voltages  $\vec{V}_{\text{ref}}$  given for the tank containing only water. The reference measurements are first used to solve for the unknown electrode contact impedances and the conductivity of water in the tank. This is done by minimizing the following sum-of-squares objective function

$$F(\vec{B}) = 10^6 \sum_{j=1}^{M_L} \left| V_{\text{num}}^j(\vec{B}) - V_{\text{exp}}^j \right|^2, \quad (9)$$

where  $\vec{B} := (z_1, \dots, z_{32}, \sigma_0)$  contains the contact impedances  $z_k$  and the conductivity of water  $\sigma_0$ , and where  $V_{\text{exp}}$  are the experimentally measured voltages. Here  $M_L$  is the number of available voltage measurements at the challenge Level  $L$  and  $\vec{V}_{\text{num}}(\vec{B})$  denotes the numerically found voltages. The factor  $10^6$  in (9) increases the effectiveness of the optimization algorithms we use: the minimization of  $F$  is done by using MATLAB's `fmincon`-function. In this work, we chose to use the default optimization algorithm of `fmincon` called 'interior-point' algorithm. In general it is a second-order algorithm, requiring information of the objective function's gradient and Hessian. After the contact impedances and the conductivity of water are found, we record the numerically obtained voltages  $\vec{V}_{\text{num}}^0$  at the minimum of the objective function  $F$ . We then calculated the voltage discrepancy

$$\delta\vec{V} := \vec{V}_{\text{ref}} - \vec{V}_{\text{num}}^0,$$

and used it to correct the voltage measurement for all of the challenge problems as

$$\vec{V}_{\text{corrected}} := V_{\text{exp}} - \delta\vec{V}.$$

At all of the challenge levels we then minimized the objective function

$$F_{\text{corrected}}(\vec{B}) := 10^6 \sum_{j=1}^{M_L} \left| V_{\text{num}}^j(\vec{B}) - V_{\text{corrected}}^j \right|^2,$$

that is, the expression (9) with  $\vec{V}_{\text{exp}}$  replaced by  $\vec{V}_{\text{corrected}}$ . In the challenge levels, the quantity  $\vec{B}$  denotes the parameters involved in the parametrizations of the interfaces  $\partial\Omega_i$ , and their conductivities. In our reconstructions we used two different types of curves: smooth curves and convex polygons. To parametrize smooth curves (e.g., ellipses, blobs) we used finite sums of trigonometric functions (essentially truncated Fourier series), while polygons were parametrized by arc length given the vertices of the polygon. Moreover, trigonometric interfaces are parametrized so that the resulting curves are star-shaped and non-self-intersecting. We note that restricting to two Fourier “coefficients” results in ellipses; the largest number of Fourier coefficients we employ here is five. We should thus note that for many of the displayed bodies the shape *can not* be identified by our putative smooth curves, and that the findings are approximations to the desired shapes within our (very) finite dimensional space of allowed curves. In case of polygonal interfaces, we only take the vertices defining the convex hull of the polygon. This is done both to allow one to “hide” more vertices within the convex hull during optimization and to prevent the interfaces from self-intersecting. A downside to this approach is that we cannot reconstruct non-convex polygons, for example, the star-shaped polygons appearing in KTC2023 at Levels 2B, 3A, 6B, and 7A.

It can be noted that this approach requires accurate simulation of the voltages arising in EIT, because we directly minimize the squared voltage differences. In Figure 1 we have plotted the given experimental voltages against the numerically arising voltages for two of the challenge data sets. This figure also shows the difference in amount of data available at Level 0 when using all of the 32 electrodes against Level 7, where 12 electrodes are disabled.

### 3.3 Results

We have performed a set of experiments on the provided data. In the initial guesses we used the *a priori* knowledge of the number of inclusions inside the water chamber and also in some cases that the inclusions are known to be polygonal. This information was *not available* to the participants. Moreover, the initial guesses have been set taking into account the location of inactive electrodes. While our choice of initial guess was done by hand, one could implement an automatic choice of initial guess by employing first another method, such as the d-bar or monotonicity based methods, thresholding the resulting first reconstruction, and finally parametrizing the interfaces arising from thresholding.

This task will be addressed in future research. By contrast, in Figure 5 we show the results of some reconstructions where the number of bodies is guessed incorrectly. For more reconstructions with incorrect initial assumptions, we refer to [25]. The results are depicted in Figures 2, 3, and 4. The initial guesses are shown in grey dotted line, while the found location of inclusion is given in red solid line. The active electrode locations at the outer boundary are marked with red color, while the electrodes not used for measurement are marked with black. The ground truth’s yellow inclusions are more and teal inclusions less conductive compared to the background water.

We also present the found conductivities for each case in the Table 1. In the reconstructions we allowed the bodies overlap not only with other inclusions, but also with the outer boundary under the condition that the conductivity of an inclusion covering an entire electrode is non-zero – otherwise we cannot guarantee solvability of the CEM equations. Any parts of an inclusion outside of the domain of reconstruction are discarded from the system of equations (8). We used varying number of parameters in our initial guesses. In case of polygons, we sometimes included more vertices (hidden inside the convex hull) than visible, so that the initial guess might initially look like a square, but later evolve into a more complicated shape (see for example Figure 2 Target A, where a square evolves into a pentagonal shape.). Similarly, in many other cases we started with an initial guess of a disc, which we allowed to evolve into an ellipse or more complicated shape by using higher number of trigonometric functions (see for example Figure 3 Target B at Levels 2 and 4). Above each reconstruction in Figures 2, 3, and 4 we show the “Score”, that is, the objective function value

$$\text{Score} := F(\vec{B}_{\text{found}})$$

where  $\vec{B}_{\text{found}}$  denotes the located inclusions in the end. Roughly speaking, we conclude that a low Score (i.e., objective function value, displayed above each reconstruction) of around 1000 to 4000 is, visually, a “good reconstruction”, while scores higher than that tend to correspond to visually poor quality reconstructions.

*Remark 1.* In our initial findings we observed a consistent visual discrepancy between our reconstructions and the provided ground truth pictures; visually it seemed that the ground truths were consistently shrunk by a fixed factor, see Figure 6. We communicated our findings with the KTC2023 organizers who confirmed a rescaling was needed. In this paper we thus compare our reconstructions with the *updated* ground truth figures.

Level	Target	Found conductivities					
0	A	0.0042	90.86	0			
0	B	0.0042	34.99	0			
0	C	0.0042	3.1938				
0	D	0.0045	0				
1	A	0.0042	0				
1	B	0.0041	2215.16				
1	C	0.0045	0				
2	A	0.0042	625.49				
2	B	0.0044	0				
2	C	0.0042	0.0198	84.25			
3	A	0.0045	0	0			
3	B	0.0042	0				
3	C	0.0042	0.0318				
4	A	0.0043	0	115.43			
4	B	0.0042	0	3.2553			
4	C	0.0043	0	0.9172			
5	A	0.0042	0.0186	0	0.5430	0	
5	B	0.0042	0				
5	C	0.0043	0.1627	117.49			
6	A	0.0043	0.6879	0.0238	0	0.2445	
6	B	0.0044	0	0	7.2893		
6	C	0.0043	0.7856	0			
7	A	0.0045	0	20.83	0	0.0267	
7	B	0.0043	0	0	0	2.4173	
7	C	0.0043	0	0			

Table 1: The found conductivities listed for the reconstructions appearing in Figures 2–4, the first number being the found conductivity of water. The conductivities will need to be scaled by depth of water to get real (3D) units. We conclude that the resistive inclusions are found to be perfect insulators, while conductive bodies appear essentially perfect conductors (relative to water).

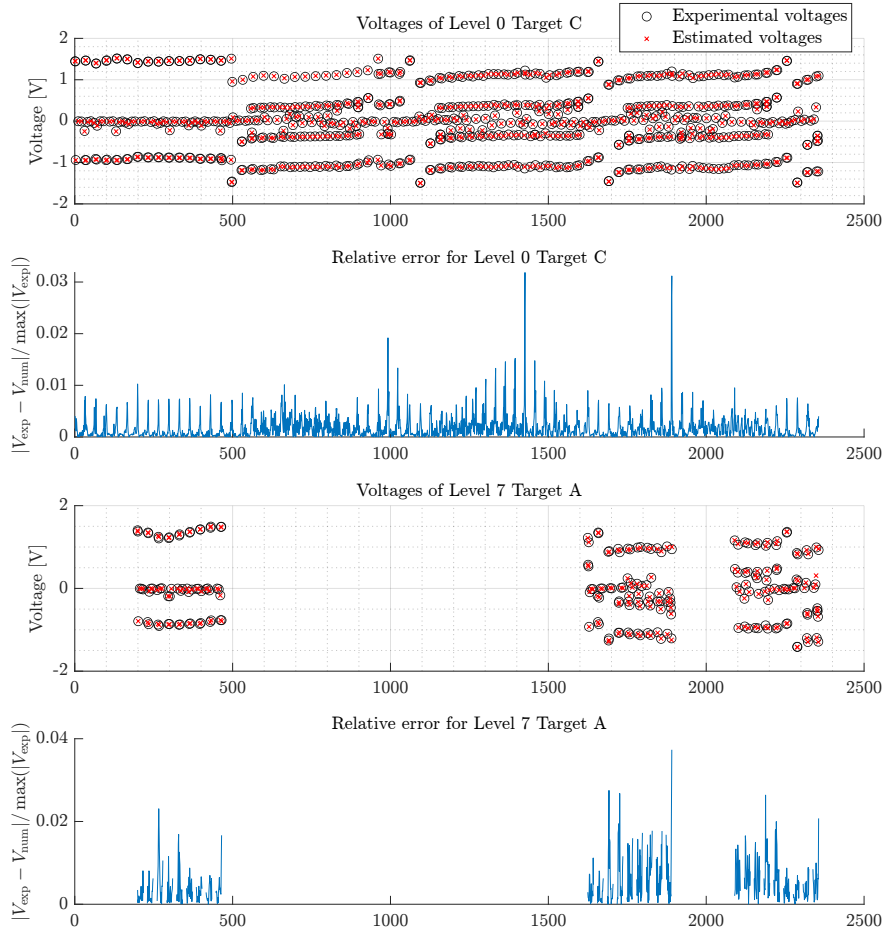


Figure 1: Comparison of the available experimental voltages (black circles) and the numerically estimated voltages (red crosses) which correspond to the voltages one *would* have, assuming the found solution from the inverse solver. The first figure shows the measured voltages corresponding to the 3rd target of Level 0 (32 electrodes; example data given to the participants). Here the full 2356 measurements are available. Below, in the third plot we show the 513 available voltages in the case of the first target at Level 7 (12 electrodes disabled; challenge data unavailable to participants). The second and fourth plots show the respective relative errors  $|V_{\text{exp}} - V_{\text{num}}| / \max(|V_{\text{exp}}|)$  for these two cases. Here  $V_{\text{exp}}$  and  $V_{\text{num}}$  are the experimentally measured and numerically found voltages, respectively. As most measured voltages are small, for visual clarity we display all voltages above the threshold of 0.3 V in absolute value, but only every 5<sup>th</sup> voltage below 0.3 V.

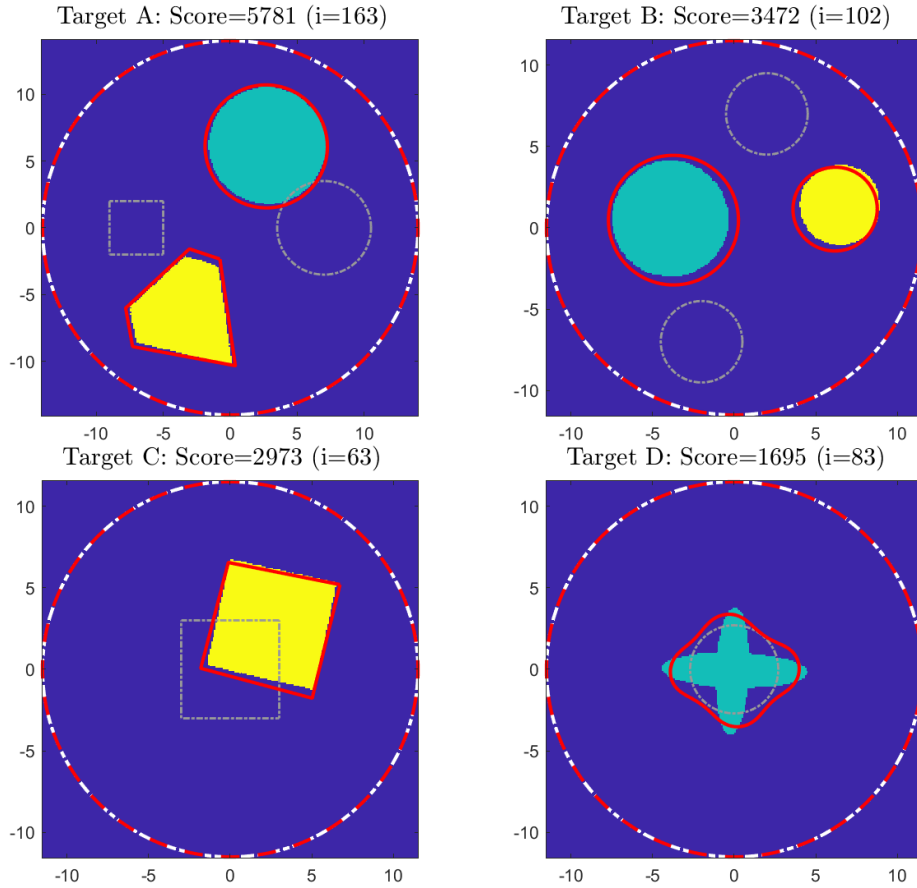


Figure 2: Level 0: Full data available. The ground truth's yellow inclusions are more and teal inclusions less conductive compared to the background water, respectively. Numerically found location of inclusions in solid red line and the initial guess in grey dotted line. Score above each image is the objective function value at the end and  $i$  denotes the number of iterations the optimizer took. We emphasize that in case of Target A we start with an initial guess on the left that contains five vertices, whose convex hull is a square. The optimizer then finds a better fit to the data by employing all of the five vertices, by finding a pentagonal diamond shape.

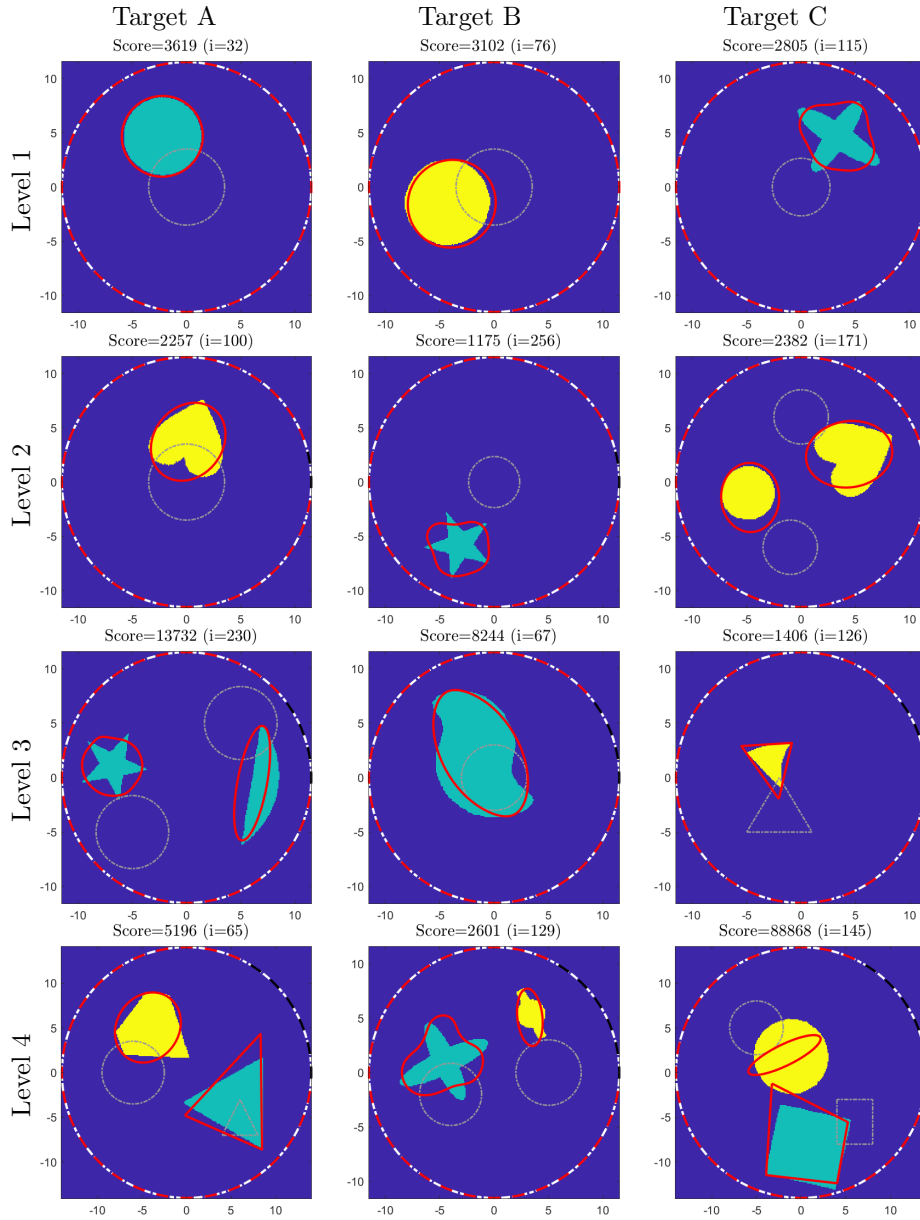


Figure 3: Full 32 electrode data at Level 1 and reducing the number of voltage measurements by 2 electrodes at each increment of level of difficulty. The active electrode locations at the outer boundary are marked with red color, while the electrodes not used for measurement are marked with black. The ground truth's yellow inclusions are more and teal inclusions less conductive compared to the background water. Numerically found location of inclusions in solid red line and the initial guess in grey dotted line. Score above each image is the objective function value at the end and  $i$  denotes the number of iterations the optimizer took.

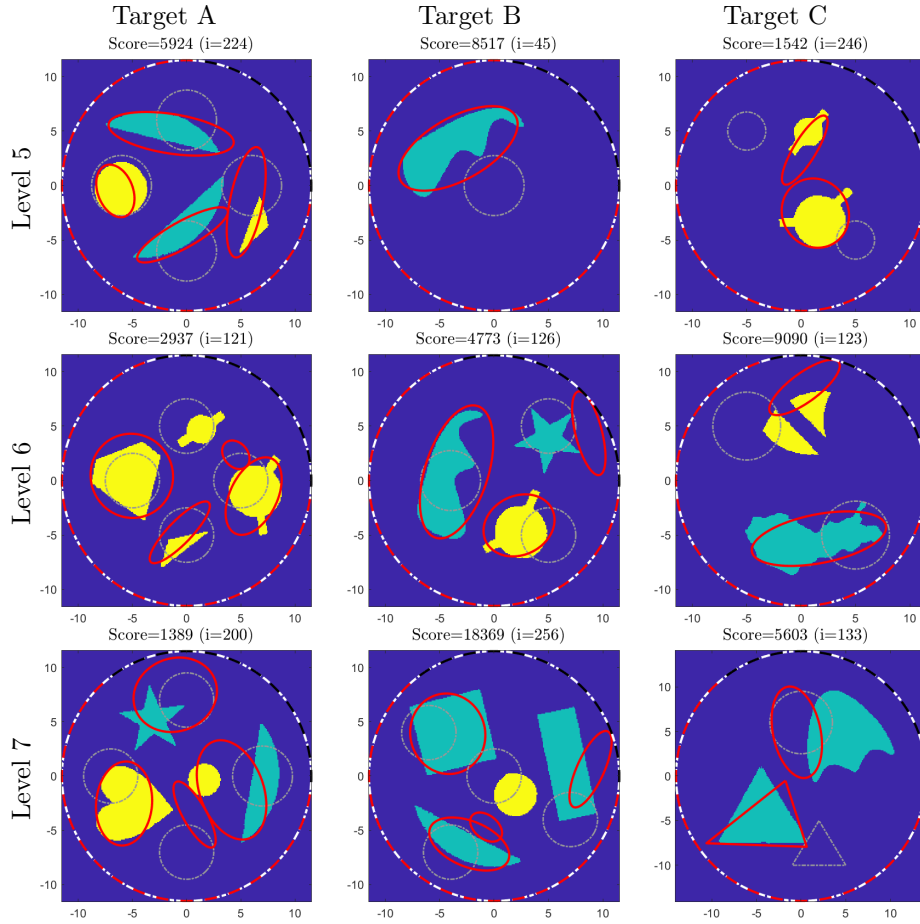


Figure 4: The active electrode locations at the outer boundary are marked with red color, while the electrodes not used for measurement are marked with black. The ground truth's yellow inclusions are more and teal inclusions less conductive compared to the background water. Numerically found location of inclusions in solid red line and the initial guess in grey dotted line. Score above each image is the objective function value at the end and  $i$  denotes the number of iterations the optimizer took.

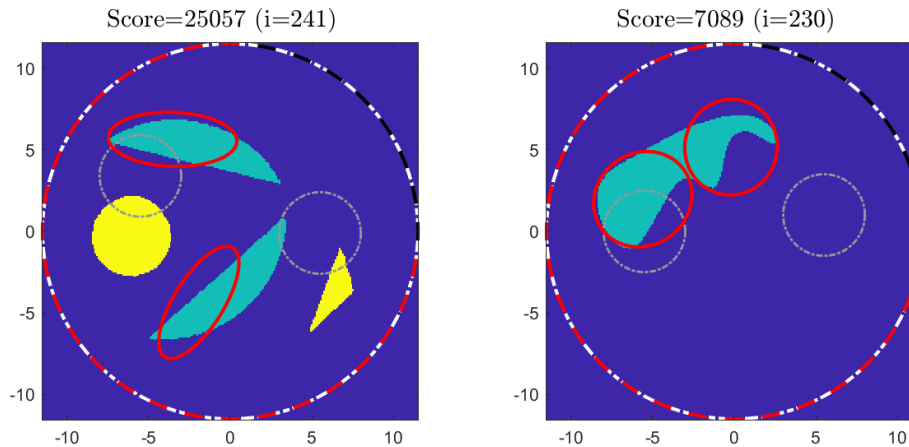


Figure 5: Level 5: Targets A and B, 8 removed electrodes, 1012 voltage measurements. In these examples we are forcing an initial guess with incorrect number of bodies. The ground truth’s yellow inclusions are more and teal inclusions less conductive compared to the background water. Numerically found location of inclusions in solid red line, and the initial guess in grey dotted line. Score above each image is the objective function value at the end and  $i$  denotes the number of iterations the optimizer took.

## Acknowledgements

S. Alexakis and A. Stinchcombe were supported by the Natural Sciences and Engineering Research Council of Canada (NSERC): RGPIN-2020-01113 and RGPIN-2019-06946. T. Tyni was supported by the Research Council of Finland (Flagship of Advanced Mathematics for Sensing, Imaging and Modelling grant 359186) and by the Emil Aaltonen Foundation.

## References

- [1] J. Agnelli, V. Kolehmainen, M. Lassas, P. Ola, and S. Siltanen. Simultaneous reconstruction of conductivity, boundary shape, and contact impedances in electrical impedance tomography. *SIAM J. Imaging Sci. (SIIMS)*, 14(4):1407–1438, 2021.
- [2] J.P. Agnelli, A. Cöl, M. Lassas, R. Murthy, M. Santacesaria, and S. Siltanen. Classification of stroke using neural networks in electrical impedance tomography. *Inv. Probl.*, 36(11):115008, 2020.
- [3] K.Y. Aristovich, B.C. Packham, H. Koo, G.S.D. Santos, A. McEvoy, and D.S. Holder. Imaging fast electrical activity in the brain with electrical impedance tomography. *NeuroImage*, 124:204–213, 2016.

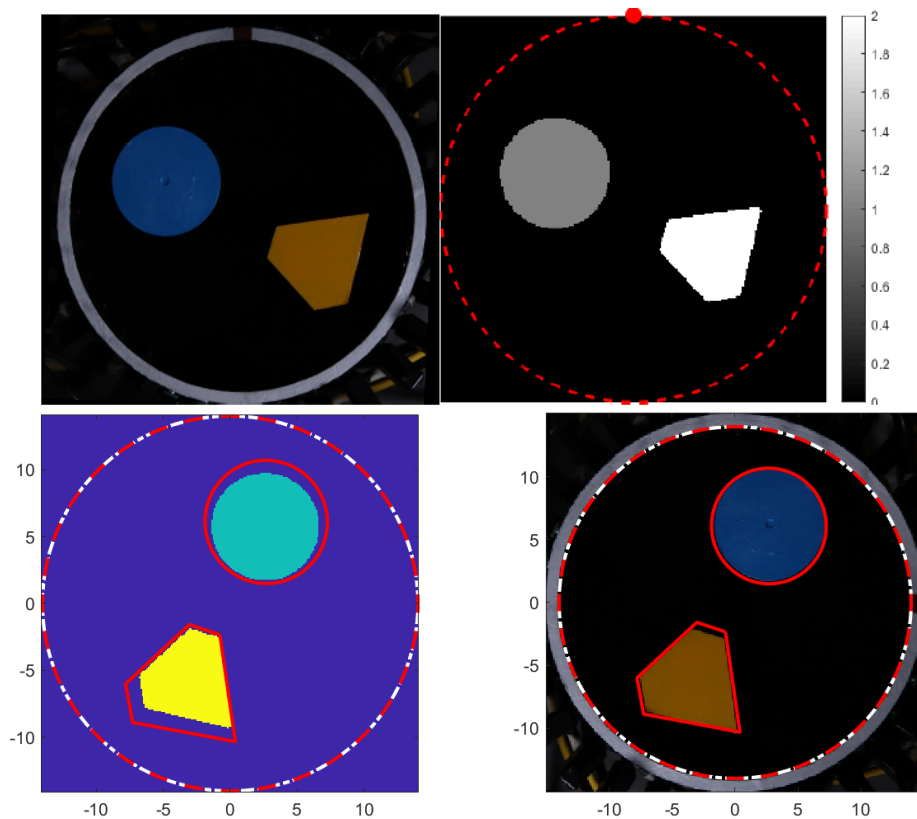


Figure 6: Top: Figure 2 of [20]. Photograph of the water tank (left) with two target phantoms inside and the *original* ground truth picture provided to the contestants (right). Visually, it appears the boundary of the domain is mismatched in the ground truth compared to the inner boundary of the water chamber. This is confirmed by overlapping the two images in a picture editing software. Bottom: A reconstruction against the original ground truth (left), and same reconstruction plotted over the photograph of the water chamber while matching the inner boundary of the water tank with the domain of reconstruction (right). Visually, the inclusions are more accurately located in the right picture. We refer to Figure 2 for more detailed view of the reconstruction against the updated ground truth figures.

- [4] G. Boverman, T.J. Kao, R. Kulkarni, B.S. Kim, D. Isaacson, G.J. Saulnier, and J.C. Newell. Robust linearized image reconstruction for multifrequency EIT of the breast. *IEEE Trans. Med. Imag.*, 27:1439–1448, 2008.
- [5] K. Bower, K. Serkh, S. Alexakis, and A. R. Stinchcombe. Fast computation of electrostatic potentials for piecewise constant conductivities. *arXiv: 2205.15354*, 2022.
- [6] James Bremer, Zydrunas Gimbutas, and Vladimir Rokhlin. A nonlinear optimization procedure for generalized Gaussian quadratures. *SIAM J. Sci. Comput.*, 32(4):1761–1788, 2010.
- [7] V. Candiani, A. Hannukainen, and N. Hyvönen. Computational framework for applying electrical impedance tomography to head imaging. *SIAM J. Sci. Comput.*, 41(5):B1034–B1060, 2019.
- [8] E. T. Chung, T. F. Chan, and X.-C. Tai. Electrical impedance tomography using level set representation and total variational regularization. *Journal of Computational Physics*, 205(1):357–372, 2005.
- [9] C. Constanda, D. Doty, and W. Hamill. *Boundary integral equation methods and numerical solutions*, volume 232. Springer, 2016.
- [10] John Crow. Quadrature of integrands with a logarithmic singularity. *Math. Comput.*, 60(201):297–301, 1993.
- [11] Fabrice Delbary and Rainer Kress. Electrical impedance tomography with point electrodes. *J. Integral Equ. Appl.*, 22(2):193–216, 2010.
- [12] Fabrice Delbary and Rainer Kress. Electrical impedance tomography using a point electrode inverse scheme for complete electrode data. *Inv. Probl. Imag.*, 5(2):355–369, 2011.
- [13] Harry Eckel and Rainer Kress. Non-linear integral equations for the complete electrode model in inverse impedance tomography. *Appl. Anal.*, 87(10-11):1267–1288, 2008.
- [14] Johan Helsing and Rikard Ojala. Corner singularities for elliptic problems: Integral equations, graded meshes, quadrature, and compressed inverse preconditioning. *J. Comput. Phys.*, 227(20):8820–8840, 2008.
- [15] D. Isaacson, J. Mueller, J.C. Newell, and S. Siltanen. Reconstructions of chest phantoms by the d-bar method for electrical impedance tomography. *IEEE Trans. Med. Im.*, 23:821–828, 2004.
- [16] D. Isaacson, J. Mueller, J.C. Newell, and S. Siltanen. Imaging cardiac activity by the d-bar method for electrical impedance tomography. *Physiol. Meas.*, 27:843–850, 2006.
- [17] R. Kress. *Linear integral equations*, volume 82. Springer, 3 edition, 2014.

- [18] N. Mandache. Exponential instability in an inverse problem for the Schrödinger equation. *Inv. Probl.*, 17:1435–1444, 2001.
- [19] K. Paulson, W. Breckon, and M. Pidcock. Electrode modelling in electrical impedance tomography. *SIAM J. Appl. Math.*, 52:1012–1022, 1992.
- [20] M. Räsänen, P. Kuusela, J. Jauhiainen, M. Arif, K. Scheel, T. Savolainen, and A. Seppänen. Kuopio tomography challenge 2023 (ktc2023). 2023.
- [21] M. Räsänen, P. Kuusela, J. Jauhiainen, M. Arif, K. Scheel, T. Savolainen, and A. Seppänen. Kuopio tomography challenge 2023 open electrical impedance tomographic dataset (ktc 2023) [data set], 2023.
- [22] E. Somersalo, M. Cheney, and D. Isaacson. Existence and uniqueness for electrode models for electric current computed tomography. *SIAM J. Appl. Math.*, 52(4):1023–1040, 1992.
- [23] Lloyd N. Trefethen. *Approximation Theory and Approximation Practice, Extended Edition*. SIAM, Philadelphia, PA, 2019.
- [24] Lloyd N. Trefethen and J. A. C. Weideman. The exponentially convergent trapezoidal rule. *SIAM Review*, 56(3):385–458, 2014.
- [25] T. Tyni, A. R. Stinchcombe, and S. Alexakis. A boundary integral equation method for the complete electrode model in electrical impedance tomography with tests on real-world data. *SIAM J. Imag. Sci.*, 17, 2024.
- [26] G. Uhlmann. Electrical impedance tomography and Calderón’s problem. *Inv. Probl.*, 25(12):123011, 2009.

E-mail addresses:

Spyros Alexakis: alexakis@math.toronto.edu  
 Adam Stinchcombe: stinch@math.toronto.edu  
 Teemu Tyni: teemu.tyni@oulu.fi